2D Materials

PAPER

# Exploring few and single layer $CrPS_4$ with near-field infrared spectroscopy

Sabine N Neal[1], Kenneth R O'Neal[1], Amanda V Haglund[2], David G Mandrus[2,3], Hans A Bechtel[4], G Lawrence Carr[5], Kristjan Haule[6], David Vanderbilt[6], Heung-Sik Kim[6,7,*] and Janice L Musfeldt[1,8,*]

[1] Department of Chemistry, University of Tennessee, Knoxville, TN 37996, United States of America
[2] Department of Materials Science and Engineering, University of Tennessee, Knoxville, TN 37996, United States of America
[3] Materials Science Technology Division, Oak Ridge National Laboratory, Oak Ridge, TN 37831, United States of America
[4] Advanced Light Source Division, Lawrence Berkeley National Laboratory, Berkeley, CA 94720, United States of America
[5] National Synchrotron Light Source II, Brookhaven National Laboratory, Upton, NY 11973, United States of America
[6] Department of Physics and Astronomy, Rutgers University, Piscataway, NJ 08854, United States of America
[7] Department of Physics, Kangwon National University, Chuncheon 24341, Republic of Korea
[8] Department of Physics and Astronomy, University of Tennessee, Knoxville, TN 37996, United States of America
* Authors to whom any correspondence should be addressed.

**E-mail:** heungsikim@kangwon.ac.kr, musfeldt@utk.edu, heungsikim@kangwon.ac.kr and musfeldt@utk.edu

**Keywords:** $CrPS_4$, van der Waals solid, exfoliated monolayer, ultra-thin limit, near-field infrared spectroscopy, symmetry analysis, polar and chiral materials, symmetry crossover

Supplementary material for this article is available at online

OPEN ACCESS

RECEIVED
23 January 2021

REVISED
14 March 2021

ACCEPTED FOR PUBLICATION
26 March 2021

PUBLISHED
26 April 2021



## Abstract

We combine synchrotron-based near-field infrared spectroscopy and first principles lattice dynamics calculations to explore the vibrational response of $CrPS_4$ in bulk, few-, and single-layer form. Analysis of the mode pattern reveals a $C2$ polar + chiral space group, no symmetry crossover as a function of layer number, and a series of non-monotonic frequency shifts in which modes with significant intralayer character harden on approach to the ultra-thin limit whereas those containing interlayer motion or more complicated displacement patterns soften and show inflection points or steps. This is different from $MnPS_3$ where phonons shift as $1/size^2$ and are sensitive to the three-fold rotation about the metal center that drives the symmetry crossover. We discuss these differences as well as implications for properties such as electric polarization in terms of presence or absence of the P–P dimer and other aspects of local structure, sheet density, and size of the van der Waals gap.

## 1. Introduction

Work on complex van der Waals systems has begun to encompass materials beyond the scope of traditional transition metal dichalcogenides leading to the discovery of diverse monolayer systems [1, 2]. At the forefront of this exciting initiative lies the transition metal trichalcogenide $MPS_3$ ($M$ = Mn, Fe, and Ni) family of materials. These systems are attracting particular attention (1) as candidate multiferroics [3], (2) for their tunability under external stimuli such as pressure, magnetic field, and temperature [4–11], (3) for their ease of exfoliation [12–16], and (4) as platforms for studying magnetism in the ultra-thin limit [10, 12, 17–22]. Monolayers of $MnPS_3$, $FePS_3$, and $NiPS_3$ display quite different functionalities including magnetism, electron-phonon coupling, and symmetry breaking [10, 12, 17–20, 22]. Extension to related members of the series including $CrPS_4$ and $CuInP_2S_6$ will enhance our understanding of these properties and, at the same time, allow for the development of structure-property relations.

$CrPS_4$ is a closely related analog that differs from the $MPS_3$ ($M$ = Mn, Fe, Ni) family in (1) stoichiometry as well as (2) lack of a phosphorus-phosphorus dimer. The latter promotes dissimilar stacking patterns and therefore different symmetry effects as well as distinct local structure. $CrPS_4$ sports a $C2$ space group at room temperature [23–27], different from that in the $MPS_3$ materials ($C2/m$ for $M$ = Mn, Fe and $P\bar{3}1m$ for $M$ = Ni) [22, 28–30]. An oxidation state analysis indicates charges of $S^{2-}$, $Cr^{3+}$, and $P^{5+}$, different from the situation in $MnPS_3$ where we have $S^{2-}$, $Mn^{2+}$, and

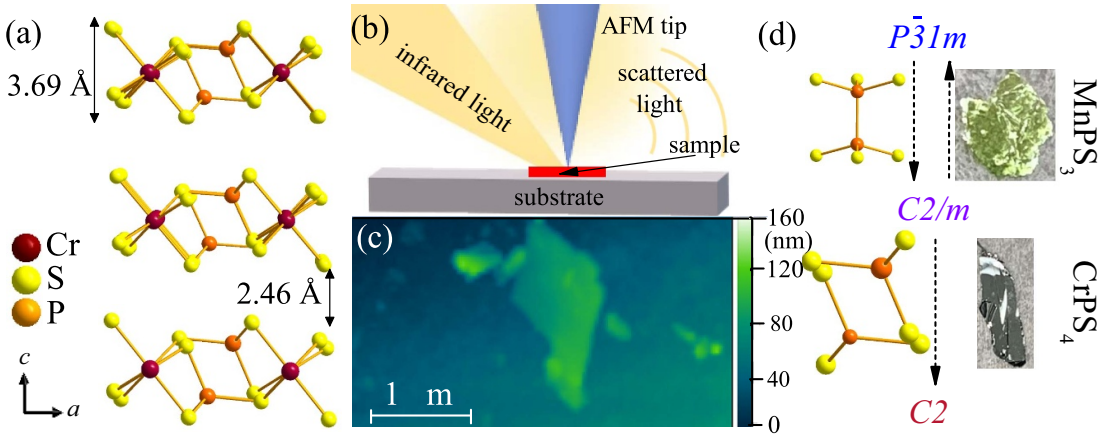


**Figure 1.** (a) Crystal structure of $CrPS_4$ at 300 K [23]. The sheet thickness and size of the van der Waals gap are indicated. (b) Schematic of the near-field infrared technique in which an atomic force microscope (AFM) cantilever tip directs light to the sample surface. (c) High resolution AFM image of exfoliated $CrPS_4$. (d) Schematic diagram of the symmetry subgroup relationships as they pertain to the presence or absence of a phosphorus dimer.

$P^{4+}$—although in this case, the P–P dimer should be considered as a unit with its own charge. The quasi-two-dimensional structure of $CrPS_4$ is characterized by puckered sulfur layers which lie parallel to the chromium and phosphorus atoms (figure 1(a)). Each $Cr^{3+}$ ($S = 3/2$) ion is coordinated by six sulfur atoms in the form of a slightly distorted octahedron, whereas the phosphorus atoms lie at the center of sulfur tetrahedron to form $[PS_4]^{3-}$-like anions [23, 24, 31]. There is no P–P dimer. The van der Waals gap is ≈2.46 Å, and the sheet thickness is 3.69 Å. At room temperature, bulk $CrPS_4$ is semiconducting (with a band gap of ≈1.4 eV) [31] and is both polar and chiral (based upon a $C2$ space group, which is the structural consensus at the present time) [24–27, 32]. Thus far, it is not known whether the system is ferroelectric (switchable) or pyroelectric (not switchable). Promising photoconductivity [33] as well as synaptic plasticity in Ag/$CrPS_4$/Ag capacitors has been observed [31]. $CrPS_4$ is a collinear antiferromagnet below $T_N = 36$ K [24, 34] with ferromagnetic interactions within the layers and weak antiferromagentic interactions between sheets [25–27]. Moreover, pressure drives an insulator to metal transition above 15 GPa [35]. Raman scattering reveals peculiar frequency vs. layer number trends, although the origin of these effects is unclear at this time [14]. Further, the vibrational modes that drive $CrPS_4$ into a polar phase have not been identified. Infrared vibrational spectroscopy combined with complementary lattice dynamics calculations is well-suited to resolving these issues in the single crystal as well as in the few- and single-layer limit.

There is, however, an important challenge that prevents a straightforward experiment to reveal the odd-symmetry infrared-active phonons in ultra-thin two-dimensional systems. Exfoliated monolayers are limited in size and therefore require high spatial resolution in order to carry out a measurement. Traditional infrared spectroscopy is not suitable for this purpose because it cannot be focused beyond the diffraction limit which is on the order of $d = \lambda/NA$. Here, $\lambda$ is the wavelength of light, and NA is the size of the numerical aperture [36]. Previously, both traditional and tip-enhanced Raman scattering spectroscopies were used to explore the even-symmetry vibrational modes of few- and single-layer sheets [10, 14, 15, 37, 38]. That said, infrared-active phonons are crucially important for unraveling certain functionalities including ferroelectricity. This is because polar (odd-symmetry) modes are needed to create a polar displacement. Synchrotron-based near-field infrared nanospectroscopy offers a way forward by overcoming the diffraction limit and providing the high sensitivity needed to measure samples with small lateral area [39–43]. Currently, the achievable spatial resolution at the Advance Light Source, Lawrence Berkeley National Laboratory is on the order of 20 × 20 $nm^2$, and the frequency window is 330–4000 $cm^{-1}$. The low frequency range from 330 to 700 $cm^{-1}$ is well suited for work on chalcogenides [40, 42, 44]. Figure 1(b) shows a schematic view of the near-field process. Here, infrared light is focused onto an atomic force microscope (AFM) cantilever tip which acts as an antenna, enhancing the electric field in the region of the tip apex. As the tip rasters across the surface, light is scattered back and collected to generate an infrared spectrum. The AFM component of this set-up is also used to determine the thickness (and therefore number of layers) of the exfoliated sheets. It also provides simultaneous output of high resolution AFM images that we use to locate candidate scan areas (figure 1(c)).

In order to extend recent spectroscopic studies of complex chalcogenides [20, 22], we measured the near-field infrared response of $CrPS_4$ in bulk,

few-, and single-layer form. We compare our findings with complementary lattice dynamics calculations as well as prior work on the $MPS_3$ family of materials ($M$ = Mn, Fe, Ni) revealing surprising differences in symmetry behavior stemming, in part, from the lack of a phosphorus–phosphorus dimer in $CrPS_4$. For example, both $MnPS_3$ and $FePS_3$ display a $C2/m$ to $P\bar{3}1m$ symmetry crossover upon approach to the monolayer due to restoration of the three-fold axis of rotation about the metal center [20]. Much like $NiPS_3$ (which remains in the $P\bar{3}1m$ space group at all thicknesses) [22], $CrPS_4$ resists distortion, maintaining its symmetry elements from the bulk to the monolayer. On the other hand, $CrPS_4$ displays complicated peak position vs. layer number trends, where some modes redshift and others blueshift. This is contrary to theoretical calculations that predict all vibrational modes blueshift on approach to the ultra-thin limit—an effect that we link with the in- vs. out-of-plane character of the mode displacement pattern. Importantly, the system retains all of its phonons to the monolayer, neither gaining or losing any. This proves to be significant because $C2$ symmetry is maintained along with symmetry-derived properties such as polarity and chirality [25, 26, 32]. For instance, our computations predict that electric polarization in a $CrPS_4$ monolayer is in-plane and on the order of 0.04 $\mu$C cm$^{-2}$. $CrPS_4$ is therefore likely to be multiferroic—once magnetic order is established.

## 2. Methods

### 2.1. Crystal growth

Single crystals of $CrPS_4$ were grown using chemical vapor transport methods as described previously [14]. Powder x-ray diffraction, energy dispersive x-ray analysis, and magnetization measurements were completed to verify crystal structure, stoichiometric composition, and magnetic ordering temperature, respectively.

### 2.2. Spectroscopy

For traditional infrared absorption and Raman scattering measurements, the single crystal was either thinned to a desired optical density or top-surface-exfoliated and adhered to a round pinhole aperture. Traditional far-field infrared studies were performed using a Bruker IFS 113v Fourier transform infrared spectrometer equipped with a bolometer detector over the frequency range of 20–700 cm$^{-1}$ with a resolution of 2 cm$^{-1}$. The measured transmittance $\mathcal{T}(\omega)$ was converted to absorption as $\alpha(\omega) = -(1/d)\ln(\mathcal{T}(\omega))$, where $d$ is the thickness. Raman scattering was carried out on a LabRAM HR Evolution Raman spectrometer (50–700 cm$^{-1}$) using an excitation wavelength of 532 nm at a power of 0.1 mW with an 1800 line mm$^{-1}$ grating. In preparation for near-field studies, single crystals were mechanically exfoliated and applied to gold substrates immediately prior to measurements. Near-field infrared spectroscopy was performed using a commercially available nanoscope (neaSNOM, Neaspec GmbH) at the Advanced Light Source, Lawrence Berkeley National Lab. This setup is available at Beamline 2.4. A Ge:Cu bolometer detector equipped with low noise components, a silicon beamsplitter, and a nitrogen enclosure enabled extension into the far infrared [40]. Both amplitude and phase data were collected across the available frequency range (330–700 cm$^{-1}$). Repeated measurements were conducted to confirm stability over the measurement period. AFM mapping to identify an ideal measurement area, as well as sheet thickness studies was completed as described in prior work [20, 22].

### 2.3. Lattice dynamics and structural relaxation calculations

First principles density functional theory (DFT) calculations were performed with Vienna ab-initio Simulation Package (VASP) [45, 46]. All calculations were carried with relaxations of internal atomic coordinates. Eight different types of magnetic configurations were tested in this study, and as a representative magnetic order, the intra-chain-FM-inter-chain-AF phase which was proposed to be the magnetic ground state [25] was employed for the presentation of main computational results. Basic structural relaxations and calculations of phonon modes were carried out using the PBEsol exchange-correlation functional [47] and the simplified rotationally-invariant flavor of the DFT+$U_{\mathrm{eff}}$ ($U_{\mathrm{eff}}$ = 2.5 eV for Cr $d$-orbital) method [48]. An 8 × 10 × 6 Monkhorst-Pack grid and up to 600 eV of energy cutoff were employed. In addition, for a detailed investigation of the polar phase, the Strongly Constrained and Appropriately Normed (SCAN) semilocal density functional [49] was used for comparison with the conventional Ceperley-Alder [50] and Perdew–Burke–Ernzerhof [51] functionals. Also, an optimized form of van der Waals correction (optB86b scheme as implemented in VASP) was employed to compute exfoliation energies and to check possible van der Waals effects on structural and magnetic properties of $CrPS_4$ [52]. For the calculations in the single-layer limit, a vacuum thickness of 18 Å was used. Additional computational details are available in the supporting information (available online at stacks.iop.org/2DM/8/035020/mmedia) [53].

## 3. Results and discussion

### 3.1. Vibrational spectroscopy and mode assignments of $CrPS_4$

Figure 2 summarizes the vibrational properties of $CrPS_4$ at room temperature. In addition to traditional far field infrared absorption, Raman scattering, and the near-field infrared spectrum of the bulk single crystal, it also displays theoretically-predicted mode

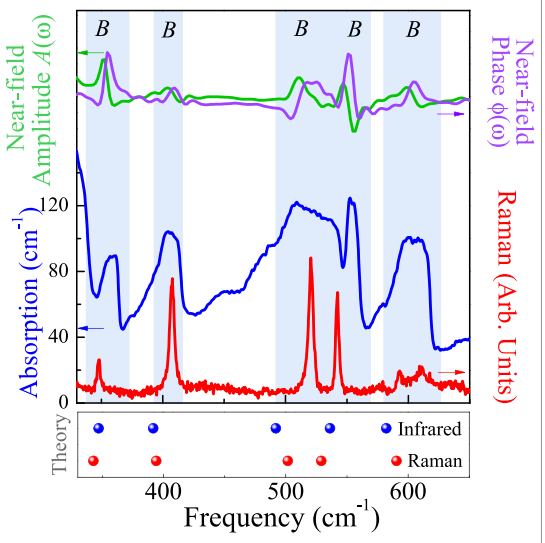


**Figure 2.** Synchrotron-based near-field infrared spectrum of single crystalline $CrPS_4$ as compared to traditional far field infrared absorption (blue) and Raman scattering (red) spectra at room temperature. Both amplitude (green) and phase (violet) of the near-field response are shown. The mode symmetries are labeled above the near-field spectra. The bottom panel displays theoretically predicted phonon frequencies for the *C*2 space group.

positions and symmetry assignments. We assign the spectral features by comparison with our theoretical lattice dynamics calculations and prior literature results [54, 55]. These assignments are summarized in table S1, and the displacement patterns are shown in figures S2 and S3, supporting information. Comparison of the traditional infrared absorption and Raman scattering response immediately reveals overlapping phonons—exactly what is expected in the non-centrosymmetric *C*2 space group [14, 23–26]. Group theory predicts that $CrPS_4$ has vibrational symmetries of $\Gamma = 17A + 19B$, with all modes being both infrared and Raman active. Prior Raman scattering spectroscopies are well in line with this symmetry analysis [14], although specific mode assignments were missing until now. These assignments are important for understanding specific local lattice distortions and structure-property trends as a function of layer number. We assign the infrared-active vibrational modes at 407, 523, 554, and 605 $cm^{-1}$ as well as the Raman-active vibrational modes near 407, 521, 543, 592, and 610 $cm^{-1}$ as various motions of the $PS_4$ unit. The infrared active phonon at 360 $cm^{-1}$ is related to a Cr–S asymmetric stretch, whereas the Raman active feature near 347 $cm^{-1}$ is attributed to out-of-plane Cr translation + sulfur in-plane motion. There are a number of additional Cr-containing modes at lower frequencies—below the 330 $cm^{-1}$ low-frequency cutoff of the detector.

Figure 2 displays the near-field infrared spectrum of the $CrPS_4$ single crystal. Both amplitude and phase are shown. The peak positions and shapes are in excellent agreement with the traditional infrared features, so mode assignments are made by comparison with the far field data. The phonons in this frequency range are primarily due to different types of P–S motion—aside from the low frequency near-field infrared mode at 355 $cm^{-1}$ which is ascribed to an asymmetric Cr–S stretch. Complete assignments, symmetries, and displacement patterns are provided in the supporting information (table S1, figures S2 and S3). Having placed the $n = \infty$ member on a firm foundation, we can bring these mode assignments and symmetries together with near-field infrared spectroscopy of exfoliated $CrPS_4$ to uncover symmetry changes on approach to the ultra-thin limit.

### 3.2. Toward few- and single- sheet $CrPS_4$

Figure 3 summarizes the near-field infrared response of $CrPS_4$ as a function of layer number, *n*. Strikingly, a comparison of bulk vs. monolayer spectra in figure 3(a) shows a similar pattern. Mode frequencies from first principles calculations in the lower part of the panel correlate well with both the bulk and monolayer features. Theory predicts that all of the infrared-active *B* symmetry modes in this system harden—by different degrees—on approach to $n = 1$. Figures 3 (b) and (c) display the evolution of the near-field response as a function of layer number. The presence of all five features in the monolayer spectrum and the fact that no new modes arise suggests that there is in fact no symmetry crossover, meaning that the bulk and the monolayer exist in the same *C*2 (polar and chiral) space group [32]. Therefore, polar character is maintained in the ultra-thin limit. This finding supports prior Raman studies, in which it was revealed that there is indeed no symmetry crossover [14].

Theory also indicates that vibrational mode frequencies should blueshift on approach to the ultra-thin limit (lower panel, figure 3(a)). This trend is presumably an expression of the changing interlayer interaction. Spectra of bulk and exfoliated $CrPS_4$ allow us to test this supposition. Surprisingly, we find that mode behavior is more complicated than predicted. The key to unraveling these trends is to examine the mode displacement patterns in terms of in- vs. out-of-plane motion.

Figure 4 summarizes frequency vs. layer number trends in $CrPS_4$. In general, the peak positions of all five vibrational modes are fairly consistent until $n < 20$. Below this critical length scale, the feature near 410 $cm^{-1}$ decreases in amplitude rapidly as it blue shifts on approach to the monolayer. Though much less intense, this structure is still noticeable in the $n = 1$ spectra and is slightly red shifted. The phonon near 605 $cm^{-1}$ hardens systematically with decreasing layer number while remaining fairly consistent in both size and shape. Near $n = 10$, there is a noticeable step with a dramatic frequency upshift, relaxation, and then further hardening with decreasing layer number. The overall size of the blue

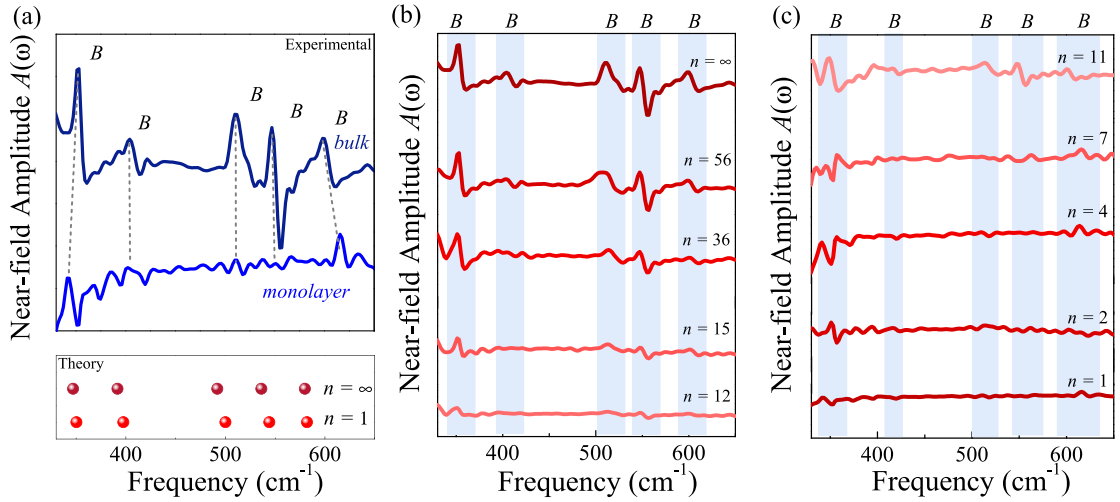


**Figure 3.** (a) Near-field infrared response of bulk and monolayer $CrPS_4$ along with theoretically predicted infrared-active mode positions for both $n = \infty$ and $n = 1$. (b), (c) Progression of the near-field infrared response of $CrPS_4$ from bulk to the monolayer. *B* symmetry phonon positions are marked by vertical blue bands.

shift from $n = \infty \rightarrow 1$ is rather large, on the order of 17 $cm^{-1}$. This corresponds to a change in the force constant of approximately 1%. The overall hardening of the 410 and 605 $cm^{-1}$ phonons is in line with our first principles calculations. Though these modes show an overall blue shift, neither has the 1/sheet thickness$^2$ dependence expected for a simple confinement model.

While the 410 and 605 $cm^{-1}$ phonons blue shift with decreasing $n$, other modes show more complicated behavior (figure 4). For instance, the mode at 552 $cm^{-1}$ hardens slightly and retains both intensity and shape until $n = 11$. At the same time, the frequency reaches a maximum near $n = 11$ before softening toward $n = 1$. The 552 $cm^{-1}$ mode starts to lose intensity as well. Turning to the low frequency mode centered near 355 $cm^{-1}$, the overall trend is for a slight red shift with decreasing layer number. The amplitude drops as well. However, there is a frequency up-shift at $n \leqslant 4$. Lastly, we focus on the 521 $cm^{-1}$ peak. We again see an initial red shift, followed by a marked frequency upturn below $n = 10$. The intensity of this feature drops below $n = 36$, although the mode is still present in the monolayer.

Analysis of the displacement patterns for the five vibrational modes of interest in $CrPS_4$ reconciles these trends (figure 4). Starting with the simple cases, analysis reveals that the displacement pattern of the 610 $cm^{-1}$ mode contains primarily in-plane motion; this feature hardens systematically with decreasing layer number. By contrast, the 552 $cm^{-1}$ mode consists of mostly out-of-plane motion; it softens with decreasing $n$. This is perhaps expected as out-of-plane motion is easier when a layered material is thinner. The other three phonons (355, 410, and 450 $cm^{-1}$) contain both in- and out-of-plane displacements. These modes exhibit complex trends, first hardening (softening) and then softening (hardening). Overall, as $n$ decreases, in-plane motions blueshift whereas out-of-plane motions redshift. As a result, modes that contain both in- and out-of-plane motions display a combination of effects resulting in a reversal of behavior at some critical thickness. These trends are consistent with findings from previous $CrPS_4$ sheet studies employing Raman scattering [14]. Prior work, however, did not fully unravel these trends likely because mode assignments and displacement patterns were not studied. We therefore find that out-of-plane aspects of the displacement pattern become more important with decreasing $n$ and dominate in the $n = 1$ material. This makes sense because interlayer interactions are eliminated in the ultra-thin limit.

### 3.3. Structure-property relations and the absence of the phosphorus-phosphorus dimer

Prior work on the $MPS_3$ ($M$ = Mn, Fe, Ni) family of materials reveals different symmetry trends from the bulk $\rightarrow$ few $\rightarrow$ single sheet. A $C2/m$ to $P\bar{3}1m$ symmetry transition occurs at room temperature due to the presence of a phosphorus–phosphorus dimer [22]. Different symmetry constraints are present at low temperature [21]. In the $MnPS_3$ and $FePS_3$ systems, it is the loss of the $B_u$ symmetry mode near 450 $cm^{-1}$ that reveals the symmetry crossover. This mode is a phosphorus-phosphorus stretch combined with a $PS_3$ translation. In the Mn system, this symmetry crossover occurs below $n = 11$, whereas the Fe analog has a crossover region between $n = 17$ and 10 [22]. Furthermore, symmetry lifting is a result of restoration of the three-fold rotation axis, meaning that in both the Mn and Fe cases, the single layer belongs to a higher-order space group ($P\bar{3}1m$) than the bulk crystal ($C2/m$) [20, 28–30, 56]. The $B_u$ mode is not present in the Ni bulk infrared spectra nor is there a

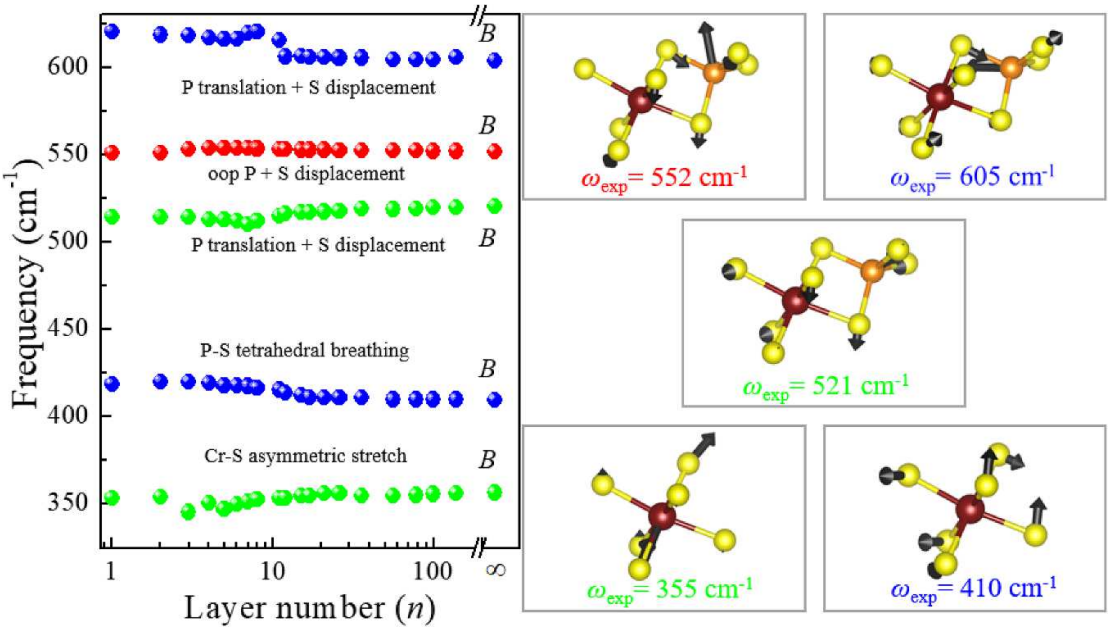


**Figure 4.** Mode frequencies (obtained from the near-field infrared spectra in figure 3) as a function of layer number along with theoretically predicted displacement patterns. The blue data points are representative of mostly in-plane motions, red is mostly out-of-plane motions, and green represents a combination of in- and out-of-plane motions.

loss or gain of spectral features as a function of layer number [22]. Therefore $NiPS_3$ remains $P\bar{3}1m$ at all $n$.

Figure 5 compares the near-field infrared vibrational response, symmetry crossover, and space group assignments for $CrPS_4$ and $MnPS_3$, respectively. The most notable difference between these two analogs is the lack of the phosphorus–phosphorus dimer in the $CrPS_4$ complex. This dimer, along with the difference in metal center and sulfur stoichiometry, gives $MnPS_3$ a $C2/m$ symmetry in the bulk and $P\bar{3}1m$ at $n = 1$. This is in contrast to the $C2$ space group of the $CrPS_4$ system at all $n$. The space groups themselves ($C2/m$ and $C2$) are both subgroups of $P\bar{3}1m$. The Mn system in its bulk form does not have the three-fold rotational axis, however below the symmetry crossover, the three-fold rotational axis about the metal center is restored. This system retains inversion symmetry to $n = 1$ (figure 5(c)). These symmetry elements are all absent in $CrPS_4$.

Also noteworthy is the fact that $CrPS_4$ has a significantly smaller van der Waals gap than $MnPS_3$ (2.46 vs. 3.27 Å). We anticipate that a system with a smaller van der Waals gap will be more difficult to exfoliate. Indeed, computed exfoliation energies of $CrPS_4$ and $MnPS_3$ employing a recently suggested method [57] and van der Waals correction are 0.41 and 0.32 eV f.u.$^{-1}$, respectively, supporting our expectation[9]. At the same time, $CrPS_4$ has (mostly) much smaller bond lengths and angles than $MnPS_3$ [53], making the *ab* plane of $CrPS_4$ more compact, though the sheet thickness along the *c* axis is larger than that in $MnPS_3$. Examination of bond lengths and angles offers further insight into the layer density for both the $CrPS_4$ and $MnPS_3$ materials. For example, the P–S bonds in $CrPS_4$ are on average 1% shorter than in the $MnPS_3$ complex. This is also true of the *M*–S bond ($M$ = Cr, Mn), where Cr–S bonds are again shorter by ≈1.1%. Following suit, the S–P–S angles are smaller in the Cr complex—on the order of 1.1%. Interestingly, the S–*M*–S angles are slightly larger in $CrPS_4$ compared to $MnPS_3$ with a significantly larger range and number of unique angles as well. Bond lengths and angles, as well as average values, are summarized in table 1. Taken together, it is likely that the more compact $CrPS_4$ layers are more rigid, resisting any change in space group, consistent with our findings.

### 3.4. Evidence for a polar ground state in $CrPS_4$

There has been significant controversy regarding the symmetry of $CrPS_4$. Originally thought to be $C2/m$ [34], more recent x-ray work supports the $C2$ space group [23–26, 32]. To clarify the symmetry, we performed DFT calculations of the bulk and single-layer $CrPS_4$ structures employing multiple exchange-correlation functionals [59]. Unexpectedly, in both structures, we find that only the SCAN metaGGA functional in the presence of spin–orbit coupling reproduces the polar structure, while results from other functionals (including SCAN without spin-orbit coupling (SOC)) converge to the centrosymmetric $C2/m$ phase. Sizes of the polar deviations from the nonpolar structures are 0.005 Å, yielding an energy gain of about 0.05 meV per formula unit at most. Because of the small

[9] PBE+optB86b+$U_{eff}$ = 4 eV was used to compute exfoliation energies of $MnPS_3$ and $CrPS_4$ in the absence of spin–orbit coupling with a vacuum thickness of 35 Å.

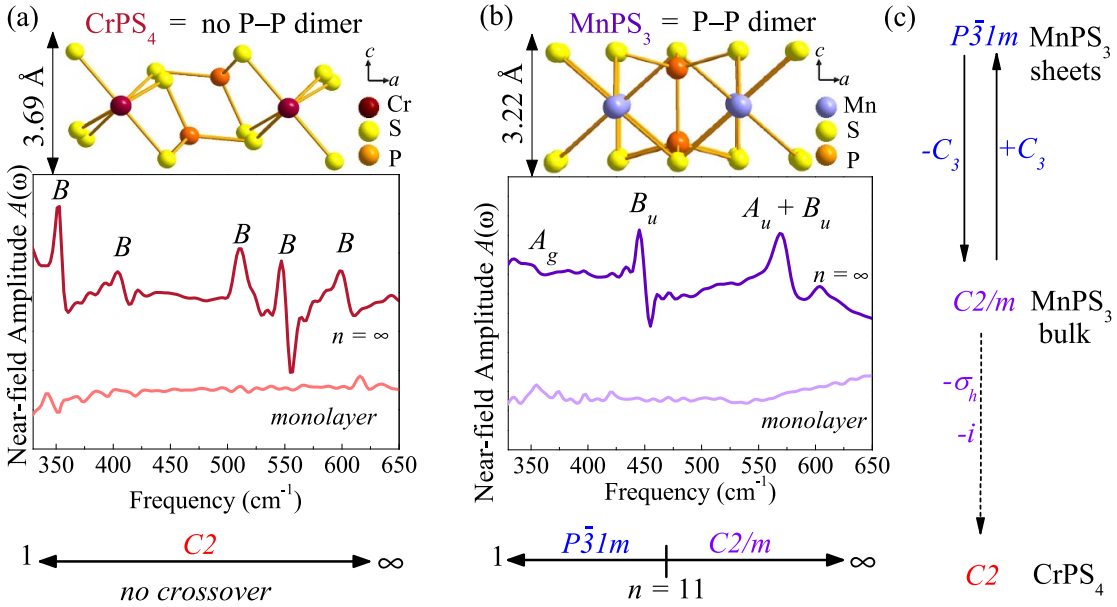


**Figure 5.** Comparison of bulk vs. monolayer (a) $CrPS_4$ and (b) $MnPS_3$ in terms of structure, spectral features, and symmetry. (c) Schematic of space group relationships for both $CrPS_4$ and $MnPS_3$ at room temperature.

**Table 1.** Summary of bond lengths and angles for $CrPS_4$ and $MnPS_3$ at room temperature. The significant figures come from the original [23, 30, 58].

| Bond/angle type | $CrPS_4$ | Number | $MnPS_3$ | Number |
|---|---|---|---|---|
| P–S bond (Å) | 2.0138 | 1 | 2.0735 | 2 |
| | 2.0198 | 1 | 2.0762 | 1 |
| | 2.0879 | 1 | | |
| | 2.0883 | 1 | | |
| Average (Å) | 2.0525 | | 2.0744 | |
| P–P bond (Å) | n/a | n/a | 2.2154 | 1 |
| *M*–S bond (Å) | 2.3640 | 2 | 2.5887 | 2 |
| | 2.4381 | 2 | 2.5942 | 2 |
| | 2.4402 | 2 | 2.5818 | 2 |
| Average (Å) | 2.4141 | | 2.5882 | |
| S–P–S angle (°) | 103.122 | 1 | 114.640 | 1 |
| | 103.221 | 1 | 114.290 | 2 |
| | 108.690 | 1 | | |
| | 108.957 | 1 | | |
| | 114.175 | 1 | | |
| | 118.777 | 1 | | |
| Average (°) | 109.490 | | 114.407 | |
| S–*M*–S angle (°) | 83.413 | 2 | 85.439 | 2 |
| | 83.835 | 1 | 85.490 | 2 |
| | 85.010 | 1 | 85.652 | 2 |
| | 87.178 | 2 | 94.150 | 2 |
| | 92.661 | 2 | 94.302 | 1 |
| | 96.357 | 2 | 94.396 | 1 |
| | 96.786 | 2 | 94.922 | 2 |
| Average (°) | 90.136 | | 90.000 | |

energy gain, manifestation of the polar phase may be suppressed to very low temperatures, or quenched entirely by zero-point fluctuations [60]. Note that loss of inversion symmetry in our optimized structure is primarily manifested in unidirectional displacements of sulfur atoms with respect to the chromium lattice along the Cr-chain direction. This is different from what was proposed in [25], where the authors suggest that staggered displacements of two bipartite Cr sublattices is the origin of the polar phase. Our

symmetry refinements show that, while this pattern is also observed in our non-SOC results, it is irrelevant to the loss of the inversion center. Details of the crystal structure optimization and displacement patterns are available in supporting information [53]. In terms of symmetry, the coexistence of spin–orbit coupling and magnetism breaks the mirror plane perpendicular to the Cr–Cr edge-sharing chain direction, leading to the loss of the inversion symmetry and the resulting polar phase. The small energy gain in the presence of electric polarization is attributed to the weak strength of spin–orbit coupling within the Cr *d*-orbitals and the resulting small spin-lattice coupling.

As discussed previously, the actual displacements that create the lower-symmetry structure are quite small, making the distinction subtle. There are important consequences of this finding, provided $CrPS_4$ indeed possesses the *C*2 symmetry. The *C*2 space group is both polar and chiral. That said, there have been no reports (to our knowledge) of either ferroelectricity (switchable polarization) or pyroelectricity (not switchable). If switchable, because our findings suggest that the bulk polar mode persists down to the single-layer limit, atomically-thin $CrPS_4$ may realize ideal two-dimensional ferroelectricity. In addition, it is well-known that coexistence of structural chirality and magnetization leads to nonreciprocal transport of quasiparticles and collective excitations [61, 62], namely diode effects. In this regard, $CrPS_4$ has the potential to be another rare example of a chiral magnet that exhibits nontrivial consequences of magnetoelectric coupling and intriguing light-matter interactions.

## 4. Summary and outlook

We employ synchrotron-based near-field infrared nanospectroscopy to explore the odd-symmetry infrared-active vibrational modes in the complex two-dimensional system $CrPS_4$ in bulk, few- and single-layer form. We compare our findings with complementary lattice dynamics calculations and prior studies on the $MPS_3$ family of materials ($M$ = Mn, Fe, Ni), revealing surprising differences in symmetry behavior. For example, $MnPS_3$ and $FePS_3$ both display symmetry crossovers, transitioning from $C2/m$ in the bulk crystal to a higher-order space group ($P\bar{3}1m$) on approach to the monolayer due to restoration of the three-fold rotation axis about the metal center. Furthermore we explore peak position vs. layer number trends in $CrPS_4$, revealing complex tendencies amongst all modes, where some modes first harden (soften) and then soften (harden). We link these trends to the in- vs. out-of-plane character of the specific mode displacement patterns. Much like $NiPS_3$, we find that $CrPS_4$ resists distortion, maintaining its symmetry elements from the bulk to the ultra-thin limit. This may be due to a number of factors including the lack of a phosphorus–phosphorus dimer in $CrPS_4$, the narrow van der Waals gap, as well as the dense, compact slab, both of which allow the system to resist distortion. This preservation of *C*2 symmetry is useful for applications because symmetry-driven properties, such as polarity and chirality, should be retained in the monolayer. For instance, we predict that the electric polarization of $CrPS_4$ is approximately 0.32 $\mu C\,cm^{-2}$ in the bulk and 0.04 $\mu C\,cm^{-2}$ in the monolayer. Taken together, our work significantly extends the understanding of symmetry breaking and local lattice distortions in complex chalcogenides, and it motivates continuing work across the broad family of two-dimensional systems.

## Data availability statement

The data that support the findings of this study are available upon reasonable request from the authors.

## Acknowledgments

Research at the University of Tennessee is supported by the Materials Science Division, Office of Basic Energy Sciences, U.S. Department of Energy, under award DE-FG02-01ER45885 (J L M). Work at Rutgers University is funded by the National Science Foundation DMREF program (DMR-1629059). A V H acknowledges the Center for Materials Processing, a Tennessee Higher Education Commission (THEC) supported Accomplished Center of Excellence, for funding the crystal growth work that provided materials for this research. D G M acknowledges support from the Gordon and Betty Moore Foundation's EPiQS Initiative, Grant GBMF9069. Portions of this work utilized beamline 2.4 at the Advanced Light Source, Lawrence Berkeley National Lab, which is a DOE Office of Science User Facility operated under Contract No. DE-AC02-05CH11231, including the remote user program from NSLS-II under Contract No. DE-SC0012704. H-S K acknowledges the Basic Science Research Program through the National Research Foundation of Korea funded by the Ministry of Education (NRF-2020R1C1C1005900) and computational resources including technical assistance from the National Supercomputing Center of Korea (Grant No. KSC-2020-CRE-0156).

## Conflict of interest

The authors declare no competing interests.

## ORCID iDs

Sabine N Neal https://orcid.org/0000-0002-6655-4079
Kenneth R O'Neal https://orcid.org/0000-0001-9149-1957

Amanda V Haglund https://orcid.org/0000-0003-3973-9577
David G Mandrus https://orcid.org/0000-0003-3616-7104
Hans A Bechtel https://orcid.org/0000-0002-7606-9333
G Lawrence Carr https://orcid.org/0000-0001-5478-964X
Kristjan Haule https://orcid.org/0000-0002-2284-1551
David Vanderbilt https://orcid.org/0000-0002-2465-9091
Heung-Sik Kim https://orcid.org/0000-0003-0691-7605
Janice L Musfeldt https://orcid.org/0000-0002-6241-823X

## References

[1] Burch K S, Mandrus D and Park J G 2018 *Nature* **563** 47–52
[2] McGuire M A 2020 *J. Appl. Phys.* **128** 051101
[3] Ressouche E, Loire M, Simonet V, Ballou R, Stunault A and Wildes A 2010 *Phys. Rev.* B **82** 100408
[4] Sivadas N, Okamoto S and Xiao D 2016 *Phys. Rev. Lett.* **117** 267203
[5] Yang H, Kim S W, Chhowalla M and Lee Y H 2017 *Nat. Phys.* **13** 931–7
[6] Pasco C M, El Baggari I, Bianco E, Kourkoutis L F and McQueen T M 2019 *ACS Nano* **13** 9457–63
[7] Haines C R, Coak M J, Wildes A R, Lampronti G I, Liu C, Nahai-Williamson P, Hamidov H, Daisenberger D and Saxena S S 2018 *Phys. Rev. Lett.* **121** 266801
[8] Harms N *et al* 2020 *npj Quantum Mater.* **5** 56
[9] Wang Y *et al* 2018 *Nat. Commun.* **9** 1914
[10] Kim K *et al* 2019 *Nat. Commun.* **10** 345
[11] Kargar F *et al* 2020 *ACS Nano* **14** 2424–35
[12] Du K Z, Wang X Z, Liu Y, Hu P, Utama M I B, Gan C K, Xiong Q and Kloc C 2016 *ACS Nano* **10** 1738–43
[13] Lee S, Choi K Y, Lee S, Park B H and Park J G 2016 *APL Mater.* **4** 086108
[14] Lee J *et al* 2017 *ACS Nano* **11** 10935–44
[15] Long G *et al* 2017 *ACS Nano* **11** 11330–6
[16] Wang F *et al* 2018 *Adv. Funct. Mater.* **28** 1802151
[17] Wang X *et al* 2016 *2D Mater.* **3** 1–9
[18] Huang B *et al* 2017 *Nature* **546** 270–3
[19] Sugita Y, Miyake T and Motome Y 2018 *Phys. Rev.* B **97** 035125
[20] Neal S N *et al* 2019 *Phys. Rev.* B **100** 075428
[21] Chu H *et al* 2020 *Phys. Rev. Lett.* **124** 27601
[22] Neal S *et al* 2020 *Phys. Rev.* B **102** 085408
[23] Diehl R and Carpentier C D 1977 *Acta Chem. Scand.* **B33** 1399–404
[24] Louisy A, Ouvard G, Schleich D and Brec R 1978 *Solid State Commun.* **28** 61–6
[25] Joe M, Lee H, Alyörük M M, Lee J, Kim S Y, Lee C and Lee J H 2017 *J. Phys. Condens. Matter* **29** 405801
[26] Zhuang H L and Zhou J 2016 *Phys. Rev.* B **94** 195307
[27] Calder S, Haglund A V, Liu Y, Pajerowski D M, Cao H B, Williams T J, Garlea V O and Mandrus D 2020 *Phys. Rev.* B **102** 024408
[28] Joy P A and Vasudevan S 1992 *J. Am. Chem. Soc.* **114** 7792–801
[29] Mathey Y, Clement R, Sourisseau C and Lucazeau G 1980 *Inorg. Chem.* **19** 2773–9
[30] Ouvrard G, Brec R and Rouxel J 1985 *Mater. Res. Bull.* **20** 1181–9
[31] Lee M J *et al* 2018 *NPG Asia Mater.* **10** 23–30
[32] Litvin D B 1986 *Acta Crystallogr.* A **42** 44–7
[33] Budniak A K, Killilea N A, Zelewski S J, Sytnyk M, Kauffmann Y, Amouyal Y, Kudrawiec R, Heiss W and Lifshitz E 2020 *Small* **16** 1905924
[34] Pei Q L *et al* 2016 *J. Appl. Phys.* **119** 043902
[35] Susilo R A *et al* 2020 *npj Quantum Mater.* **5** 58
[36] So S, Kim M, Lee D, Nguyen D M and Rho J 2018 *Appl. Spectrosc. Rev.* **53** 290–312
[37] Xiao D, Liu G B, Feng W, Xu X and Yao W 2012 *Phys. Rev. Lett.* **108** 196802
[38] Sun Y J, Tan Q H, Liu X L, Gao Y F and Zhang J 2019 *J. Phys. Chem. Lett.* **10** 3087–93
[39] Carr G L 2001 *Rev. Sci. Instrum.* **72** 1613–19
[40] Bechtel H A, Muller E A, Olmon R L, Martin M C and Raschke M B 2014 *Proc. Natl Acad. Sci.* **111** 7191–6
[41] Muller E A, Pollard B and Raschke M B 2015 *J. Phys. Chem. Lett.* **6** 1275–84
[42] Khatib O, Bechtel H A, Martin M C, Raschke M B and Carr G L 2018 *ACS Photonics* **5** 2773–9
[43] Mastel S, Govyadinov A A, Maissen C, Chuvilin A, Berger A and Hillenbrand R 2018 *ACS Photonics* **5** 3372–8
[44] Bechtel H A, Johnson S C, Khatib O, Muller E A and Raschke M B 2020 *Surf. Sci. Rep.* **75** 100493
[45] Kresse G and Furthmüller J 1996 *Phys. Rev.* B **54** 11169–86
[46] Kresse G and Joubert D 1999 *Phys. Rev.* B **59** 1758–75
[47] Perdew J P, Ruzsinszky A, Csonka G I, Vydrov O A, Scuseria G E, Constantin L A, Zhou X and Burke K 2008 *Phys. Rev. Lett.* **100** 136406
[48] Dudarev S L, Botton G A, Savrasov S Y, Humphreys C J and Sutton A P 1998 *Phys. Rev.* B **57** 1505–9
[49] Sun J, Ruzsinszky A and Perdew J P 2015 *Phys. Rev. Lett.* **115** 036402
[50] Ceperley D M and Alder B J 1980 *Phys. Rev. Lett.* **45** 566–9
[51] Perdew J P, Burke K and Ernzerhof M 1996 *Phys. Rev. Lett.* **77** 3865–8
[52] Klimeš J, Bowler D R and Michaelides A 2009 *J. Phys. Condens. Matter* **22** 022201
[53] See Supporting information at for traditional infrared and Raman spectra and tables with displacement patterns and optimized crystal structure and first-principles calculations (https://doi.org/10.1088/2053-1583/abf251)
[54] Sourisseau C, Cavagnat R, Fouassier M, Brec R and Elder S H 1995 *Chem. Phys.* **195** 351–69
[55] Temperini M, Sala O and Bernstein H 1978 *Chem. Phys. Lett.* **59** 10–2
[56] Lee J U, Lee S, Ryoo J H, Kang S, Kim T Y, Kim P, Park C H, Park J G and Cheong H 2016 *Nano Lett.* **16** 7433–8
[57] Jung J H, Park C H and Ihm J 2018 *Nano Lett.* **18** 2759–65
[58] Klingen W, Eulenberger G and Hanh H 1973 *J. Inorg. Gen. Chem.* **401** 97–112
[59] We used Cerpeley–Alder-type (CA) local density approximation [63], Perdew–Burke–Ernzerhof (PBE) parametrization of generalized gradient approximation (GGA) [51], revised PBE for crystalline solids (PBEsol) [64], and recently proposed Strongly Constrained and Appropriately Normed (SCAN) metaGGA functional [49]. van der Waals [52] and DFT+$U$ [48] corrections were also used in addition to the functionals discussed above
[60] Zhong W and Vanderbilt D 1996 *Phys. Rev.* B **53** 5047–50
[61] Cheong S W, Talbayev D, Kiryukhin V and Saxena A 2018 *npj Quantum Mater.* **3** 19
[62] Yokosuk M O *et al* 2020 *npj Quantum Mater.* **5** 20
[63] Ceperley D M and Alder B J 1980 *Phys. Rev. Lett.* **45** 566–9
[64] Csonka G I, Perdew J P, Ruzsinszky A, Philipsen P H T, Lebègue S, Paier J, Vydrov O A and Ángyán J G 2009 *Phys. Rev.* B **79** 155107